A NOISE PREDICTION TOOL FOR IAM AND AAM IN URBAN ENVIRONMENTS

R. Habing*, K.H. Lammers*, P. Admiraal*, R. Bakker*, H. Lania*, R. Aalmoes*,V.J.M.C. Vos*
*Royal Netherlands Aerospace Centre NLR (The Netherlands)

Abstract

New technologies are paving the way for Innovative and Advanced Air Mobility (IAM/AAM) like Unmanned Aerial Vehicles (UAV) and Urban Air Mobility (UAM). Numerous of such systems are being developed and the majority uses electrically driven rotors and/or propellers for thrust generation. Besides thrust, rotors and propellers also generate noise, causing annoyance for people in and around the IAM/AAM. Predicting this noise is therefore important for policy makers and developers of IAM/AAM. This paper describes the development of such a tool which is relatively fast so that e.g. policy makers can use it to predict noise along certain trajectories or define noise abatement procedures. For IAM/AAM developers a fast noise prediction tool is very useful in the concept design phase. For prediction of annoyance on the ground, it is also important to take the environment into account in which the noise propagates. This paper is therefore organized in three sections: a section about the noise source modelling, a section about the propagation model and a section showing how these predictions can be used in a Virtual Reality (VR) environment for noise annoyance perception studies.

1. NOTATION

Acronyms:

AAM	Advanced Air Mobility
BPF	Blade Passing Frequency
BPM	Brooks-Pope-Marcolini model
ENOISE	NLR’s full aircraft noise prediction tool
eVTOL	Electric Vertical TakeOff and Landing
IAM	Innovative Air Mobility
NLR	Netherlands Aerospace Centre
ROLLAC	Rotating Lifting Line Acoustic
ROLLNAX	Rotating Lifting Line Non-Axial
SPL	Sound Pressure Level
UAV	Unmanned Aerial Vehicle
URANS	Unsteady Reynolds-Averaged Navier-Stokes
VCNS	Virtual Community Noise Simulator
VR	Virtual Reality

2. INTRODUCTION

New technologies are paving the way for Innovative and Advanced Air Mobility (IAM/AAM) like Unmanned Aerial Vehicles (UAV) and Urban Air Mobility (UAM). Numerous of such systems are being developed and the majority uses electrically driven rotors and/or propellers for thrust generation. Besides thrust, rotors and propellers also generate noise, causing annoyance for people in and around the IAM/AAM. Predicting this noise is therefore important for policy makers and developers of IAM/AAM. Greenwood et. al [1] presented an overview of the challenges and opportunities for low-noise electric aircraft, with focus on eVTOL noise source mechanisms and prediction. UAV and UAM can be classified by their rotor scales with relatively low to medium i) chord Reynolds number and ii) tip Mach number, contrary to e.g. helicopters and conventional propeller aircraft (high tip Mach number) or wind turbines (high chord Reynolds number). For UAV and UAM it therefore can be expected that besides rotor tonal noise, also rotor broadband noise plays a significant role in the noise generation, but also in the noise propagation and eventually human noise annoyance perception in urban environment. Current perception research on aircraft noise allows for reproduction of aircraft sounds at an observer position on the ground, and includes typical propagation effects, such as geometric spreading, atmospheric absorption, and ground reflection. But most research assume free field between sound source and observer, and do not consider ground-situated structures or buildings. For low-flying air vehicles, especially if they are expected to fly within urban environments, these effects should also be considered as it may influence the sound level, sound character, and direction of the (perceived) sounds.

3. NOISE SOURCE MODELLING

3.1. General

The scope of the noise modelling encompasses rotor and propeller noise, i.e. jet powered IAM/AAM are not included in this tool (unlike NLR's full aircraft noise prediction tool ENOISE [8]). The noise modelling is centered around the commercially available software package FLIGHTLAB [9]. FLIGHTLAB is a state-of-the-art, finite element, component-based, selective fidelity modelling and analysis software package. Figure 1 shows NLR's low-fidelity noise source prediction tool scheme.

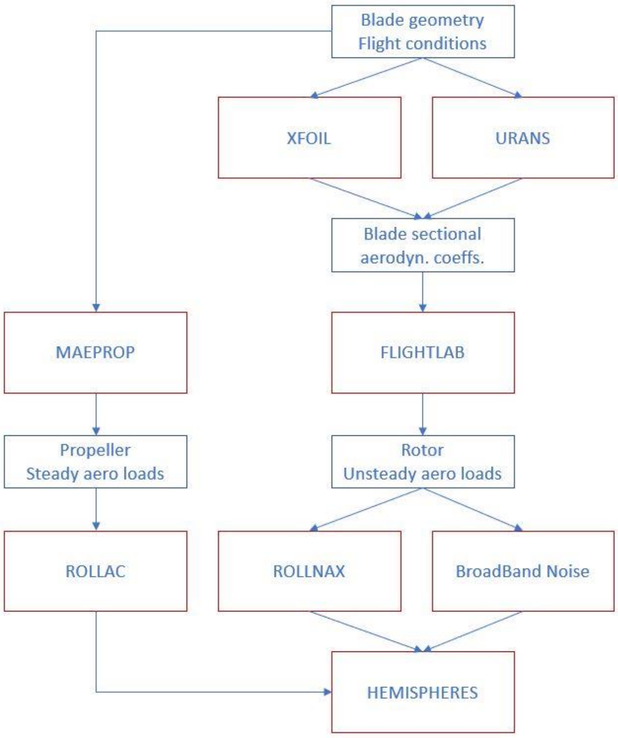

Figure 1: Flow chart of noise source prediction tool.

Starting from known blade planform geometry and flight conditions (in a wind tunnel the free-stream flow direction resembles the opposite flight direction), the blade sectional aerodynamic coefficients are obtained from either open source tool XOIL [14] or URANS simulations. FLIGHTLAB then simulates the rotor unsteady aerodynamic loads (time domain). NLR's tool ROLLNAX (Appendix A) computes the tonal noise. Rotor broadband noise is predicted by implemented semi-empirical models (i.e. BPM [4], Pegg [15], GL [16] or TI [17]). Finally, hemispheres for 1/3-octave bands present the directivity. For platforms including isolated propellers, MAEPROP [3] computes the steady aerodynamic loads and ROLLAC [3] predicts the propeller tonal noise.

Greenwood et. al [1] show an overview of the taxonomy of rotor noise sources, which is based on the work of Brooks and Schlinker [2]. Similar to this overview, the deterministic loading noise is predicted by a NLR in-house developed code called ROLLNAX (see section 7). This code is an expansion of the in-house code ROLLAC, which is developed by Brouwer [3]. The expansion covers propeller noise in non-axial flow, which is relevant for rotors and tiltrotors in IAM and AAM. The non-deterministic broadband noise is modelled with semi-empirical models, which cover blade self-noise. Turbulence and wake ingestion are not yet included in the noise toolchain.

3.2. Case study

Within this work FLIGHTLAB has been used for modelling a case study UAV (DJI Matrice M600) with blade element momentum modelling approach, see Figure 2.

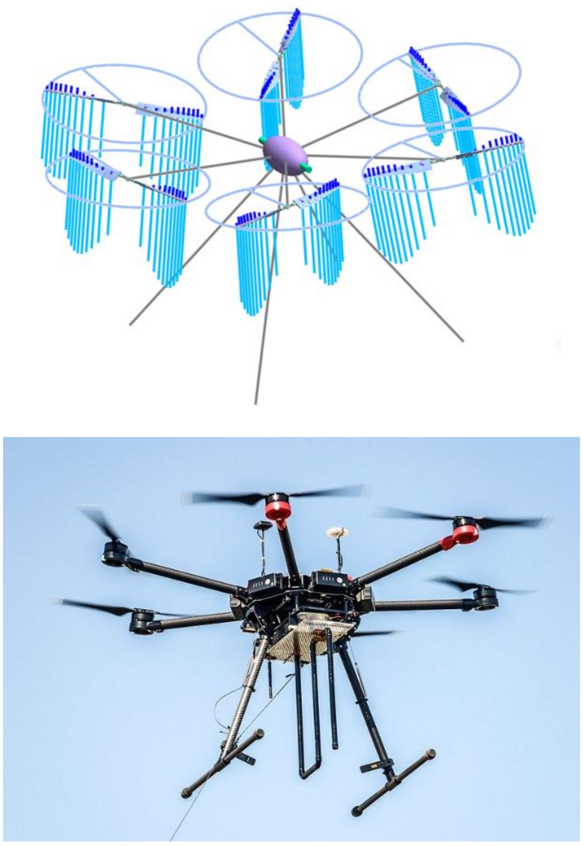

Figure 2: Top) FLIGHTLAB model of the UAV case study. Bottom) The DJI Matrice M600 [18], which is the case study UAV.

The FLIGHTLAB model provides the aerodynamic conditions at each blade section at multiple azimuth positions, whilst taking the deterministic aerodynamic interaction of the rotors onto each other into account. These aerodynamic conditions are input for the acoustic modelling. In the remaining part of this section individual steps are described.

First, the rotor blade geometry was measured by means of optical scanning. Then 10 airfoil sections were extracted to obtain chord and pitch at each spanwise position. As the airfoils appeared to have identical shape, URANS simulation were performed for this particular shape at a certain rotational speed and three Mach-Reynolds number combinations. This provided the blade sectional steady aerodynamic coefficients (lift and drag) as function of angle of attack.

Second, FLIGHTLAB simulations were performed for hover and steady flight conditions. This yielded the unsteady aerodynamic sectional loads (angle of attack, lift, drag and Mach nr at 24 azimuthal angles in the rotor plane) at trimmed rotational speed for each rotor blade and each rotor of the multi-copter. Figure 3 shows an example contour plot.

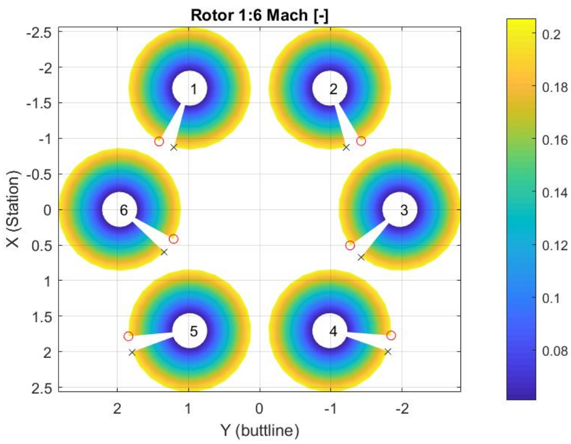

Figure 3: Contour plots of local Mach number in rotor planes during hover.

Third, the output of FLIGHTLAB was converted via an intermediate tool to required input files for ROLLNAX. It is noted that for this use case the vehicle has a longitudinal pitch and the rotor planes are positioned on a conical surface which complicated the determination of the angle between rotor-axis and flight direction (χ in Figure 11). Then the far-field version of ROLLNAX (section 7) was run to yield the tonal complex pressure at the first three BPFs on observer positions distributed over a cylindrical surface.

Fourth, the rotor broadband noise was predicted by using the BPM model [4] for identical flight conditions at identical observer positions. The implementation allows compatibility with the FLIGHTLAB output files. The output files contain SPL values for a broad range of 1/3-octave bands. Preliminary results of a comparison between the output of various semi-empirical models (section 3.1) suggest inconsistencies. The reason for this is investigated in current research.

Finally, for each flight condition the individual noise source cylinders of all rotors are summed to yield hemispheres of total SPL at specified 1/3-octave bands.

In summary, the noise of each rotor blade is calculated with varying aerodynamic loading along a blade rotation. The noise predictions for all the blades are summed and the resulting sound pressure levels on a grid surface of a hemisphere around the UAV are calculated as complex amplitudes.

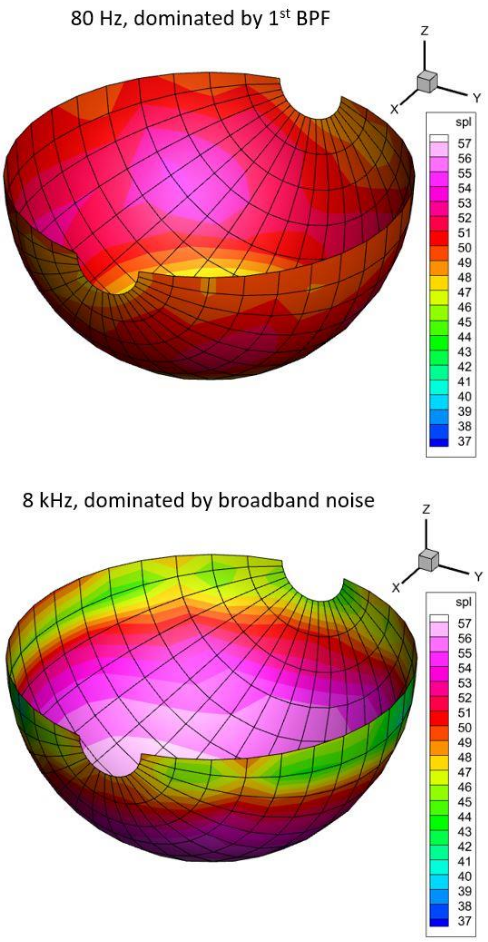

Figure 4: Examples of calculated hemispheres for a low-speed (1 knots) steady forward flight. Top) a hemisphere for the 80 Hz 1/3-octave band. Bottom) a hemisphere for the 8 kHz 1/3-octave band.

Figure 4 shows examples of two calculated hemispheres for the DJI M600 at a steady forward flight speed of 1 knots. The left hand figure is dominated by the 1st BPF, which has a strong directivity within the individual rotor planes. The right hand figure is dominated by the broadband noise, which has strong downward and upward directivity (i.e. along each rotor axis). Appendix B presents some results of a high-speed (27 knots) flyover event.

4. NOISE PROPAGATION MODELLING

The model developed in this work predicts noise propagation in an urban environment. A generic noise source description, in the form of SPL on the surface of a hemisphere encapsulating the source, forms the noise input. The urban environment is described in terms of 2D outlines of buildings accompanied with a certain height, forming blocks with flat roofs. This description is compatible with the publicly available map of the Netherlands of the RIVM [5], which is a map specifically developed for noise modelling and includes the complete map of the Netherlands. An algorithm has been developed, which finds the relevant paths between the sound source and the observer. See Figure 5.

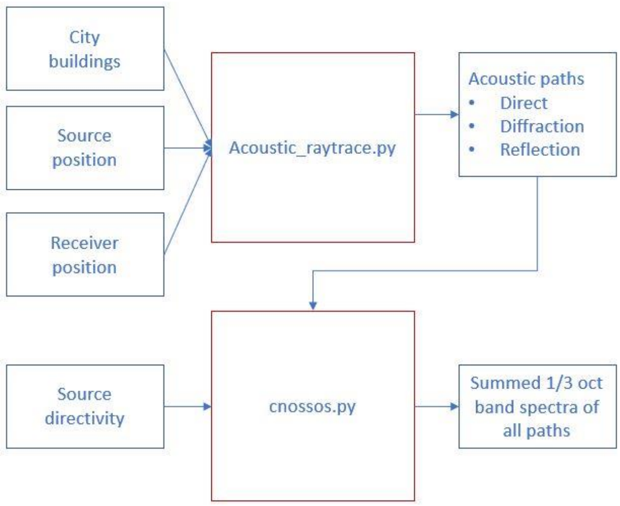

Figure 5: Flow chart of noise propagation algorithm.

This raytracing algorithm takes direct paths, diffracted paths and reflection paths into account (3 levels deep). Once the relevant paths have been found, the resulting noise level at the observer point is calculated via the method prescribed in CNOSSOS-EU [6]. Besides geometric spreading of sound power, the source directivity, atmospheric absorption, reflecting material and diffractive damping is taken into account. As use case, a flyover of the DJI Matrice M600 over the DigiCity facility at the Drone Centre of NLR [7] is modelled and corresponding noise levels on the ground are calculated, as shown in Figure 6 - Figure 8. In order to validate the tool, measurements at this facility are scheduled, but are beyond the scope of this paper.

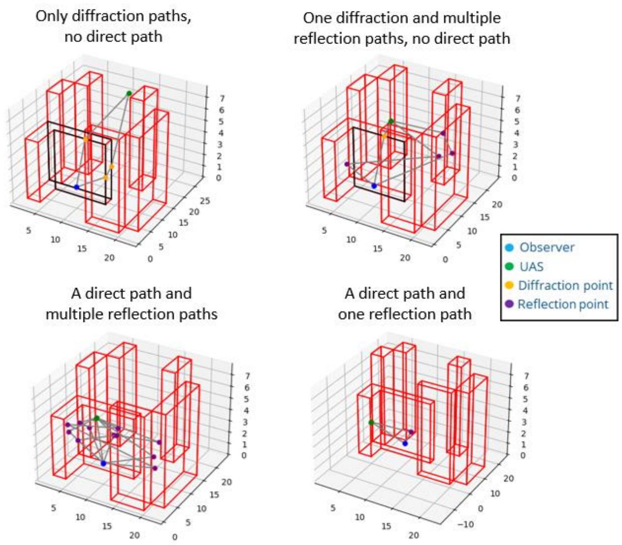

Figure 6: Visualization of calculated propagation paths for a 1 knots steady flyover at 6 meters height. From left top corner and in clockwise direction, the timestep increases, only 4 exemplary time steps are shown. The simulated urban environment concerns NLR's DigiCity.

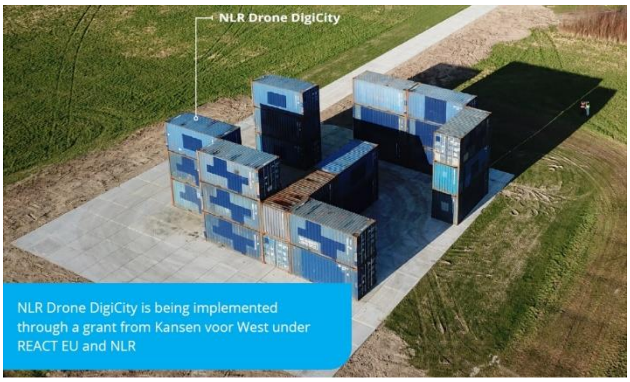

Figure 7: NLR's DigiCity for UAV urban environment studies.

The SPL evolution shows that in this case the low frequency tonal noise (rotor 1st BPF) has dominant contribution over the high frequency rotor broadband noise for the major part of the flight trajectory. From these results it is possible to directly compute an A-weighted overall SPL (analog to human perception assessment for certification-like studies). However, noise annoyance perception assessment requires additional steps that are described in the following section.

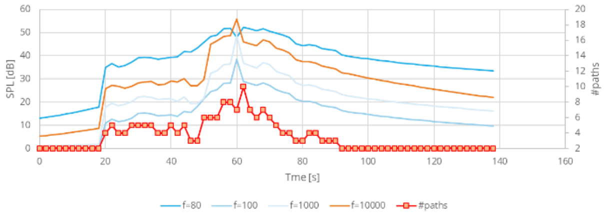

Figure 8: Calculated SPL as function of time using the hemispheres of Figure 4 and the calculated propagation paths of Figure 6 as input. The figure shows 4 different frequency bands and also shows the number of acoustic propagation paths found per timestep.

5. NOISE ANNOYANCE PERCEPTION IN A VR-WORLD

Figure 9. Person experiencing the Virtual Community Noise Simulator.

For research on noise and visual perception, NLR developed the Virtual Community Noise Simulator, a noise simulator with additional visualization using a Virtual Reality headset [10], see Figure 9. This facility allows simulation of flyover events in a controlled, laboratory setting. The simulation also allows the visualization and ambient sounds of different environments to be presented, to evaluate their impact on the participants' perception of the flyover events. There have been recent studies on the human perception of drone sounds using this simulator [11]-[12], but none of these studies considered acoustic effects on the sound propagation of drones due to the urban environment. For this reason, a model is necessary to that considers the 3D urban environment and reflection, scattering and diffraction effects on the sound propagation. In a 3D perception simulation, not only the sound as propagated through the urban environment is important, but also the direction of sound sources contribute to recreate a realistic sound simulation. In a first version of the model, focus was placed on both reflection and directivity. Scattering and diffraction shall be added in a following step.

For the simulation of drone flyover sounds in an urban environment, two approaches can be taken to simulate it in NLR's VCNS. First, if the flight path of the drone, as well as the location (or moving path) of the observer is known in advance, reflection paths can be calculated in advance. This reduces the burden of calculation while simulating the sound event. Second, using the Unity 3D game engine used in the VCNS, a virtual environment can be set up where sound paths are real-time simulated with both a moving source (drone) and a moving observer. The latter approach requires more real-time processing power and allows for interactions between drone and observer. For instance, the drone can change direction, just as the observer, and it the sound reflections will change accordingly. Note, however, that in most simulation setups, the observer will be stationary with only his or her head moving. For this reason, the noise modelling approach presented in section 4 will work if real-time processing is not required.

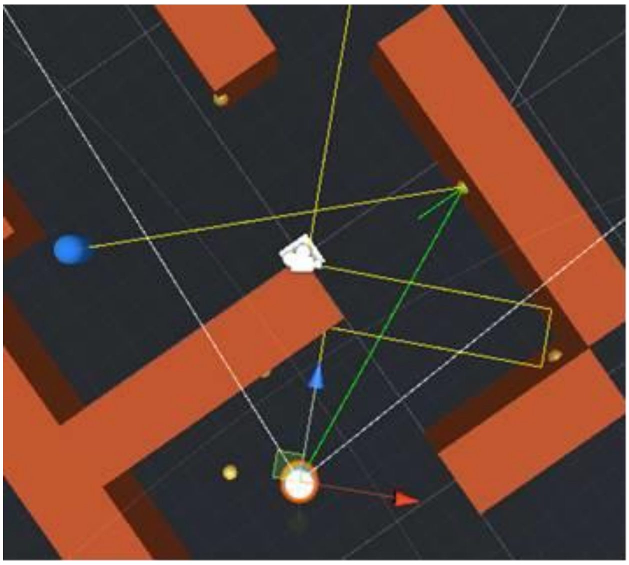

Figure 10. Top-down view of the sound paths in the Unity environment of the VCNS. The white dot is the source (drone), the blue dot is the receiver position. Brown areas are the buildings that reflect the sound. The green and yellow lines are (example) sound paths with reflections.

As a proof of concept, the real-time approach was examined as well. The idea behind this approach is that optimization improvements may lead to real-time performance later on. In this approach, the urban environment is modelled with 3D objects, and facades and ground objects are instrumented to reflect sound sources. Using ray casting functionality in the gaming engine, sound paths from drone to observer are calculated, see Figure 10. The number of real-time reflections depends on the number of facades that have been instrumented with a reflection "layer". The purpose of this layer is to add a mirroring sound source in case of a detecting of an incoming sound source. Also, additional scattering effects and diffractions were not considered as the main goal was to determine the directional paths of all reflected sources towards the observer. But future improvements may alter the reflected sound signature by applying a suitable attenuation based on the type of surface of the reflection. The Unity software allows for a visual display of these paths, making the implemented approach easier to interpret. By determining the directions, the sound can be reproduced for the receiver in the right location. This is needed as the binaural reproduction and head movements allow the observer to experience directional sounds.

6. CONCLUSIONS

1. A noise prediction tool for IAM/AAM in urban environments has been developed. The low-fidelity tool is relatively fast so that e.g. policy makers can use it to predict noise along certain trajectories or define noise abatement procedures. For IAM/AAM developers the fast prediction tool can be very useful in the concept design phase.
2. The noise modelling is centered around the commercially available software package FLIGHTLAB, where rotor-rotor and rotor-airframe aerodynamic interactions are taken into account. The rotor unsteady aero loads serve as input for the noise modelling. The deterministic loading noise is predicted by the NLR newly in-house developed code called ROLLNAX. This code is an expansion of the in-house code ROLLAC. The expansion covers propeller noise in non-axial flow, which is relevant for multi-rotor and tiltrotors in IAM/AAM. The non-deterministic broadband noise is modelled with semi-empirical models, which cover blade self-noise. Validation of these models is subject of current research. Wake ingestion and motor noise is not yet implemented in the toolchain. These are subject of current and future research.
3. FLIGHTLAB has been used for modelling a case study UAV (DJI Matrice M600). For hover and steady forward flight speed, noise hemispheres have been calculated. For low-frequency tonal noise, hemispheres per BPF show the directivity. This can be done for correlated- and uncorrelated sound sources. As multi-rotor phase information is often lacking, and RPM can vary in service, rotor uncorrelated tonal noise hemispheres are presented. It has been observed that increasing flight speed can shift the tonal directivity from largely horizontal to vertical/ground direction. The high-frequency broadband noise hemispheres show main directivity to the ground direction. This is of particular interest for human perception studies, as the A-weighing there has less penalty than the tonal noise frequency range.
4. A model has been developed for predicting noise propagation in an urban environment. The urban environment description is compatible with the publicly available map of the Netherlands. A ray-tracing algorithm takes direct-, diffraction- and reflection paths into account (3 levels deep). The resulting noise level at the observer point is calculated via the method prescribed in CNOSSOS-EU. For the case study, the SPL evolution shows dominant tonal noise (rotor 1st BPF) for the major part of the flight trajectory.
5. For research on noise and visual perception, NLR developed the Virtual Community Noise Simulator, a noise simulator with additional visualization using a VR headset. None of the recent VCNS studies on human perception of UAV noise considered acoustic effects on the sound propagation due to the urban environment. For this reason, a model has been developed that considers the 3D urban environment and noise directivity and reflection, where scattering and diffraction effects are not implemented yet.

Author contact:

remco.habing@nlr.nl

7. APPENDIX A: ACOUSTIC LIFTING-LINE MODEL FOR A ROTOR IN NON-AXIAL FLOW

A rotor in a uniform flow is considered, with the axis of the rotor making an angle χ with the flow. In this Appendix all coordinates and variables are made dimensionless on the rotor tip radius, the speed of sound, and the ambient density of air. In the lifting-line approach the wave equation for the acoustic pressure *p* and the source term can be written as ([3]):

$$\left[\left(\frac{\mathrm{D}}{\mathrm{D}t}\right)^2 - \nabla^2\right] p(x,r,\theta,t) = \frac{B}{2\pi}\sum_{n=-\infty}^{\infty} \nabla'\cdot\frac{1}{r'}\left[\vec{L} - \bar{\bar{D}}\cdot\nabla'\right].\delta(x')e^{inB(\theta'-\Omega t)} \quad (1)$$

At the left hand side a cylindrical coordinate system is used that is aligned with the main flow, i.e. a uniform flow is assumed of Mach number *M* in the positive x-direction. Here $\frac{\mathrm{D}}{\mathrm{D}t} = \frac{\partial}{\partial t} + M\frac{\partial}{\partial x}$. The cylindrical coordinate system at the right hand side is aligned with the rotor axis, i.e. the azimuthal position of a blade is given by the angle θ'. The origin coincides with the rotor plane centre. In the lifting-line approximation the sources are confined to the $x' = 0$ plane. The number of blades is denoted by *B* and the shaft rotation circular frequency by Ω. The vector $\vec{L}$ represents the force per unit span on the blades, and the tensor $\bar{\bar{D}}$ both the pitching moment and the cross-sectional area ('thickness') of the blade sections. The coordinate system is sketched in Figure 11.

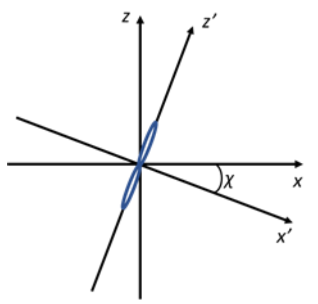

Figure 11: Coordinate system used in Eq.(1) for a rotor in non-axial flow.

In the case of a helicopter or UAV rotor, χ will be close to 90°. If $\chi = 0$, as for an aircraft propeller in level flight, the primes disappear and the same equation as in ref. [3] is retained. In that case the vector $\vec{L}$ and the tensor $\bar{\bar{D}}$ depend on the radial coordinate r only. For $\chi \neq 0$ however, they depend on both *r'* and the azimuthal position θ'. Eq.(1) can be solved by the application of a Green's function. The time dependent version of the Green's function used in ref. [3] reads:

$$G(x,r,\theta,t|\xi,\rho,\varphi,\tau) = \frac{1}{(2\pi)^2}\int_{-\infty}^{\infty} e^{i\omega(t-\tau)} \sum_{m=-\infty}^{\infty} e^{im(\theta-\varphi)} \int_0^{\infty} \frac{\gamma J_m(\gamma r) J_m(\gamma\rho)}{2i\kappa(\gamma,\omega)} \times \exp\left[i\frac{(x-\xi)}{\beta^2}\left[M\omega - \mathrm{sgn}(x-\xi)\,\kappa(\gamma,\omega)\right]\right]\mathrm{d}\gamma\mathrm{d}\omega \quad (2)$$

with:

$$\kappa(\gamma,\omega) = \omega\sqrt{1-\left(\frac{\beta\gamma}{\omega}\right)^2}, \qquad (\beta\gamma)^2 \le \omega^2$$
$$\kappa(\gamma,\omega) = -i\sqrt{(\beta\gamma)^2-\omega^2}, \qquad (\beta\gamma)^2 > \omega^2 \quad (3)$$

with $\beta = \sqrt{1-M^2}$. The time variation is trivial and the complex acoustic pressure can be written as a sum of harmonics of the BPF:

$$p = \sum_{n=-\infty}^{\infty} \bar{p}_n e^{-inB\Omega t} \quad (4)$$

After some straightforward analysis the following expression is found for the complex amplitude $\bar{p}_n$:

$$\bar{p}_n = \frac{B}{8\pi^2}\times \int_{r_h}^{1}\int_0^{2\pi}\sum_{m=-\infty}^{\infty}\int_0^{\infty} e^{i(m(\theta-\varphi)-(x-\bar{\xi})k_x+nB\varphi')}\frac{\gamma J_m(\gamma r)}{\kappa(\gamma,-nB\Omega)}$$
$$\Big\{L_\xi(\rho',\varphi')\left[\left(\frac{m}{\rho}A_{31}-k_xA_{11}\right)J_m(\gamma\rho)+i\gamma J_m'(\gamma\rho)A_{21}\right]$$
$$+L_\varphi(\rho',\varphi')\left[\left(\frac{m}{\rho}A_{33}-k_xA_{13}\right)J_m(\gamma\rho) + i\gamma J_m'(\gamma\rho)A_{23}\right]$$
$$+Q_{\xi\xi}\left[\left(\left(\frac{m}{\rho}A_{31}-k_xA_{11}\right)^2 - i\frac{m}{\rho^2}A_{31}A_{21}\right)J_m(\gamma\rho) + 2i\left(\frac{m}{\rho}A_{31}-k_xA_{11}\right)\gamma J_m'(\gamma\rho)A_{21} - \gamma^2 J_m''(\gamma\rho)A_{21}^2\right]$$
$$+Q_{\xi\varphi}\frac{nB}{\rho'}\left[\left(\frac{m}{\rho}A_{31}-k_xA_{11}\right)J_m(\gamma\rho)+i\gamma J_m'(\gamma\rho)A_{21}\right]$$
$$+\left[\frac{nB}{\rho'}Q_{\varphi\xi} - \frac{i\cos\varphi'}{\rho'}T_{\varphi\xi}\right]\left[\left(\frac{m}{\rho}A_{31}-k_xA_{11}\right)J_m(\gamma\rho) + i\gamma J_m'(\gamma\rho)A_{21}\right]$$
$$+\frac{nB}{\rho'}\left[\frac{nB}{\rho'}Q_{\varphi\varphi} - \frac{i\cos\varphi'}{\rho'}T_{\varphi\varphi}\right]A_{33}J_m(\gamma\rho)\Big\}\mathrm{d}\gamma\mathrm{d}\varphi'\mathrm{d}\rho' \quad (5)$$

with r_h denoting the radial position at the hub. It has been assumed that the tensor $\bar{\bar{D}}$ can be approximated by $\bar{\bar{D}} = \bar{\bar{Q}} + \sin\theta'\,\bar{\bar{T}}$ with $\bar{\bar{Q}}$ and $\bar{\bar{T}}$ constant in θ'. The subscripts ξ and φ denote the components in the ξ' and φ' directions. Note that if $\chi = 0$, and thus $\varphi' = \varphi$, the integration over φ yields 0, except for $m = nB$,

assuming that in this case $\vec{L}$ and $\overline{\overline{D}}$ do not depend on φ, representing a propeller in uniform flow.
The transformation from the primed to the un-primed variables is obtained by a simple coordinate transformation. By changing the integration to the primed variables the use of the Jacobian matrix $\boldsymbol{A}$ is necessary. Its components can be expressed as function of χ and φ':

$$
\begin{aligned}
A_{11} &= \frac{\partial\xi}{\partial\xi'} = \cos\chi \\
A_{12} &= \frac{\partial\xi}{\partial\rho'} = \sin\varphi'\sin\chi \\
A_{13} &= \frac{\partial\xi}{\rho'\partial\varphi'} = \cos\varphi'\sin\chi \\
A_{21} &= \frac{\partial\rho}{\partial\xi'} = \frac{-\sin\varphi'\sin\chi\cos\chi}{\sqrt{1-\sin^2\chi\sin^2\varphi'}} \\
A_{22} &= \frac{\partial\rho}{\partial\rho'} = \frac{\rho}{\rho'} = \sqrt{1-\sin^2\chi\sin^2\varphi'} \\
A_{23} &= \frac{\partial\rho}{\rho'\,\partial\varphi'} = \frac{-\sin^2\chi\cos\varphi'\sin\varphi'}{\sqrt{1-\sin^2\chi\sin^2\varphi'}} \\
A_{31} &= \frac{\rho\partial\varphi}{\partial\xi'} = \frac{-\sin\chi\cos\varphi'}{\sqrt{1-\sin^2\chi\sin^2\varphi'}} \\
A_{32} &= \frac{\rho\partial\varphi}{\partial\rho'} = 0 \\
A_{33} &= \frac{\rho\,\partial\varphi}{\rho'\,\partial\varphi'} = \frac{\cos\chi}{\sqrt{1-\sin^2\chi\sin^2\varphi'}}
\end{aligned} \tag{6}
$$

Finally, the axial wavenumber is obtained from the dispersion relation:

$$k_x = \left[MnB\Omega + \operatorname{sgn}\left(x-\bar{\xi}\right)\kappa(\gamma,-nB\Omega)\right]/\beta^2 \tag{7}$$

and

$$\bar{\xi} = \rho'\cos\varphi'\sin\chi \tag{8}$$

Far field approximation. In Brouwer [13] a different formulation for the Green's function has been applied, expressed in Bessel functions (J_n) and Hankel functions ($H_n^{(2)}$). This formulation was used to derive an approximation for large arguments, i.e. for $r \gg 1$. The same can be done here, resulting into:

$$
\begin{aligned}
&\bar{p}_n \sim \frac{B}{8\pi^2}\sum_{m=-\infty}^{\infty}\left(1-i\frac{4m^2-1}{8\gamma_0 r}\right)e^{i\frac{1}{2}\pi(1+m)} \\
&\int_{r_h}^{1}\int_{0}^{2\pi}\frac{e^{i(\alpha_0 x-\gamma_0 r)}}{\beta R}e^{i\left(m(\theta-\varphi)-\alpha_0\bar{\xi}+nB\varphi'\right)}\times \\
&\Big\{L_\xi(\rho',\varphi')\left[\left(\frac{m}{\rho}A_{31}+\alpha_0 A_{11}\right)J_m(\gamma_0\rho) + i\gamma_0 J_m'(\gamma_0\rho)A_{21}\right] \\
&+ L_\varphi(\rho',\varphi')\left[\left(\frac{m}{\rho}A_{33} + \alpha_0 A_{13}\right)J_m(\gamma_0\rho) + i\gamma J_m'(\gamma_0\rho)A_{23}\right] \\
&+ Q_{\xi\xi}\left[\left(\left(\frac{m}{\rho}A_{31}+\alpha_0 A_{11}\right)^2 - i\frac{m}{\rho^2}A_{31}A_{21}\right)J_m(\gamma_0\rho) + 2i\left(\frac{m}{\rho}A_{31}+\alpha_0 A_{11}\right)\gamma J_m'(\gamma_0\rho)A_{21} - \gamma^2 J_m''(\gamma_0\rho)A_{21}^2\right] \\
&+ Q_{\xi\varphi}\frac{nB}{\rho'}\left[\left(\frac{m}{\rho}A_{31}+\alpha_0 A_{11}\right)J_m(\gamma_0\rho) + i\gamma_0\gamma J_m'(\gamma_0\rho)A_{21}\right] \\
&+ \left[\frac{nB}{\rho'}Q_{\varphi\xi} - \frac{i\cos\varphi'}{\rho'}T_{\varphi\xi}\right]\left[\left(\frac{m}{\rho}A_{31} + \alpha_0 A_{11}\right)J_m(\gamma_0\rho) + i\gamma_0 J_m'(\gamma_0\rho)A_{21}\right] \\
&+ \frac{nB}{\rho'}\left[\frac{nB}{\rho'}Q_{\varphi\varphi} - \frac{i\cos\varphi'}{\rho'}T_{\varphi\varphi}\right]A_{33}J_m(\gamma_0\rho)\Big\}\,\mathrm{d}\varphi'\mathrm{d}\rho'
\end{aligned} \tag{9}
$$

with:

$$
\begin{aligned}
\alpha_0 &= \frac{-nB\Omega}{\beta^2}\left(M-\frac{x-\bar{\xi}}{\beta R}\right) \\
\gamma_0 &= \sqrt{(M\alpha_0 - nB\Omega)^2 - \alpha_0^2} \\
R &= \sqrt{\left(\frac{x-\bar{\xi}}{\beta}\right)^2 + r^2}
\end{aligned} \tag{10}
$$

For completeness the explicit expressions for the elements of $\overline{\overline{D}}$ are presented here (from ref. [3]):

$$
\begin{aligned}
D_{\xi\xi} &= -v_\xi^2 A + \frac{v_\xi v_\varphi}{U^2}M_p \\
D_{\xi\varphi} &= v_\xi v_\varphi A + v_\xi^2 M_p \\
D_{\varphi\xi} &= v_\xi v_\varphi A - \left(\frac{v_\varphi}{U}\right)^2 M_p \\
D_{\varphi\varphi} &= -v_\varphi^2 A - \frac{v_\xi v_\varphi}{U^2}M_p
\end{aligned} \tag{11}
$$

where A is the cross-sectional area of the blade section at ρ', M_p is the pitching moment about the intersection with the Pitch Change Axis, v_ξ and v_φ are the local flow velocity components (relative to the blade section), and $U^2 = v_\xi^2 + v_\varphi^2$.

8. APPENDIX B: NOISE SOURCE OF HIGH-SPEED STEADY FORWARD FLIGHT

This appendix presents the key results of the use case (section 3) for a high-speed (27 knots) steady flyover.

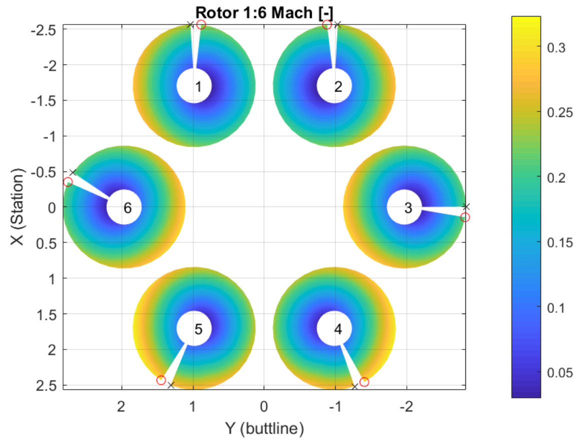

Figure 12: Contour plots of local Mach number in rotor planes during high-speed steady forward flight.

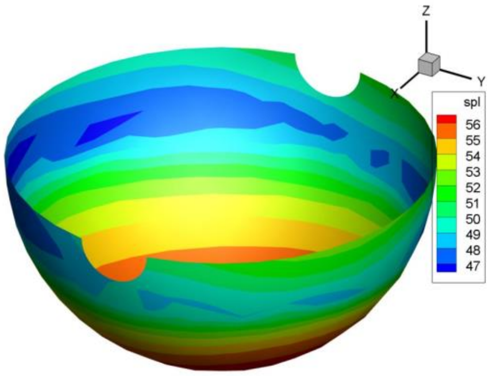

Figure 13: Hemisphere for a high-speed steady forward flight: Broadband noise at 8 kHz 1/3-oct. band.

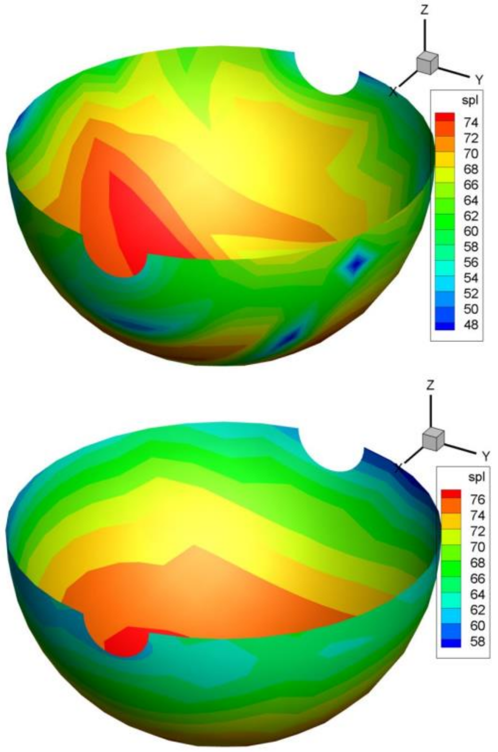

Figure 14: Hemispheres for a high-speed steady forward flight: 1st BPF. Top) correlated rotor sources. Bottom) uncorrelated rotor sources.

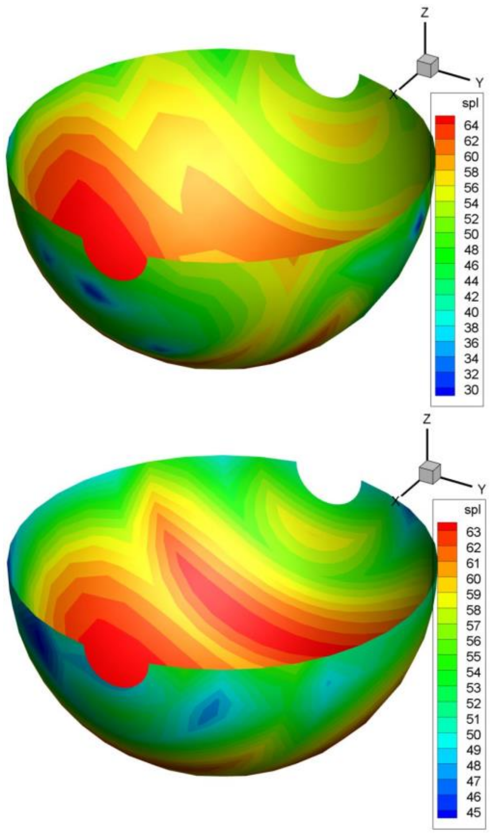

Figure 15: Hemispheres for a high-speed steady forward flight: 2nd BPF. Top) correlated rotor sources. Bottom) uncorrelated rotor sources.

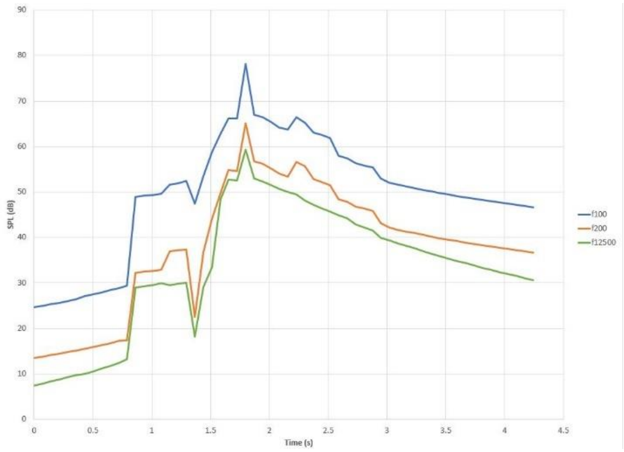

Figure 16: Calculated SPL as function of time for use case at high-speed steady forward flight in urban environment. Profiles for dominating 1/3-oct. bands are shown.

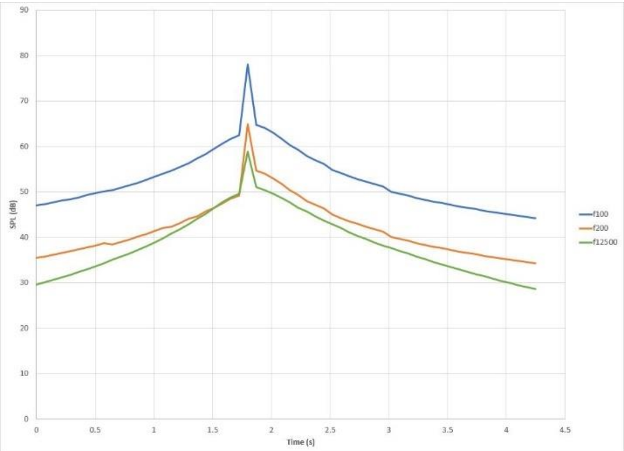

Figure 17: Calculated SPL as function of time for use case at high-speed steady forward flight in free-field. Profiles for dominating 1/3-oct. bands are shown.

9. ACKNOWLEDGMENTS

The authors like to acknowledge Dr. Harry Brouwer (NLR retired) for development of the rotor tonal noise source prediction algorithms. This work is based on early developed propeller rotating lifting line methods [3] and extended to rotor configurations (see Appendix A).

10. REFERENCES

1. Greenwood, E., Brentner, K. S., Rau, R. F., & Ted Gan, Z. F. (2022). Challenges and opportunities for low noise electric aircraft. International Journal of Aeroacoustics, 21(5-7), 315-381.

2. Brooks, T. F., & Schlinker, R. H. (1983). Progress in rotor broadband noise research. Vertica, 7(4), 287-307.

3. Brouwer, H. H. (1992). On the use of the method of matched asymptotic expansions in propeller aerodynamics and acoustics. Journal of Fluid Mechanics, 242, 117-143.

4. Brooks, T. F., Pope, D. S., & Marcolini, M. A. (1989). Airfoil self-noise and prediction (No. L-16528).

5. Kadaster. (n.d.). 3D Geluid. Retrieved November 11, 2023, from https://3dgeluid.kadaster.nl/3dgeluid/

6. Kephalopoulos, S., Paviotti, M., & Anfosso-Lédée, F. (2012). Common noise assessment methods in Europe (CNOSSOS-EU). Common noise assessment methods in Europe (CNOSSOS-EU), 180-p.

7. NLR. (n.d.). NLR Drone Digicity. Retrieved January 5, 2024, from https://www.nlr.nl/nlr-drone-digicity/

8. Van der Meulen, M.P., Knepper, K.M. & Brouwer, H.H., Translating acoustic wind tunnel data to full scale aircraft noise; Incorporation of aircraft noise models in ENOISE, NLR-CR-2016-374, 2019.

9. FlightLab. (n.d.). Home. Retrieved January 17, 2024, from https://www.flightlab.com/

10. Aalmoes R, den Boer M, Veerbeek H. Virtual Reality Aircraft Noise Simulation for Community Engagement. In: INTER-NOISE and NOISE-CON Congress and Conference Proceedings. Chicago, IL: Institute of Noise Control Engineering; 2018. p. 1559–66.

11. Aalmoes, R., Bruijn, B. de, Sieben, N., The Influence of Contextual Non-Auditory Factors on Drone Sound Perception, SAE Technical Paper 2023-01-1105, 2023, doi:10.4271/2023-01-1105.

12. Aalmoes, R., & Sieben, N. (2021). Visual and audio perception study on drone aircraft and similar sounds in an Urban Air Mobility setting. International Congress and Exposition on Noise Control Engineering, 2510–2521. https://doi.org/10.3397/IN-2021-2160

13. Brouwer, H. H., The Scattering of Open Rotor Tones by a Cylindrical Fuselage and its Boundary Layer. AIAA Paper 2016-2741, 2016.

14. Drela, M., XFOIL: An analysis and design system for low Reynolds number airfoils, Low

Reynolds number aerodynamics, Springer-Verlag Lec. Notes in Eng. 54, 1989.

15. Pegg, J., A summary and evaluation of semi-empirical methods for the prediction of helicopter rotor noise, NASA TM 80200, 1979.

16. Gill H. & Lee S., Development of new empirical rotor broadband noise prediction models for urban air mobility applications, AIAA Scitech 2024-2473, 2024.

17. Buck S., Oerlemans S. and Scott P., Experimental Validation of a Wind Turbine Turbulent Inflow Noise Prediction Code, AIAA J. Vol. 56, No. 4, April 2018.

18. www.rawpixel.com / NASA (source)